A Framed, 16-Image Kirkpatrick–Baez X-Ray Microscope

Introduction

Kirkpatrick–Baez (KB)–type[1] x-ray microscopes are one of the principal methods of imaging x-ray emission from laser-generated plasmas. They typically have a larger collecting solid angle, better spatial resolution, and larger standoff distance than the simpler method of pinhole imaging.[2] They have been used on both the 60-beam OMEGA Laser System[3] and the previous 24-beam OMEGA Laser System.[4] High spatial resolution (~3 μm) has been demonstrated using four-image KB mirror assemblies,[5] which, when framed, achieved a resolution of ~5 μm.

An advantage of using pinholes to image the plasma x-ray emission is that when coupled to a multistrip, high-speed framing camera,[6] many images can be obtained[7] with a time interval as short as ~30 ps (dictated by the separation of the pinhole images and the voltage propagation speed across the strip). Until recently, KB microscopes have been limited to just four images with larger image separation (52 mm) and corresponding longer time separations (~350 ps) when two images are coupled to a single-strip framing camera.[8] Pickworth *et al.*[9] have recently developed a KB mirror assembly for use at the National Ignition Facility[10] capable of being coupled to a four-strip, high-speed framing camera. Additionally, Yi *et al.*[11] have implemented an eight-image KB mirror assembly also coupled to a four-strip framing camera. These previous limits have been removed by the use of compact KB microscope mirrors[12] whose design has increased the number of images to 16, which, when properly aligned,[13] can be coupled to a four-strip, high-speed framing camera having strip separations of 9 mm. The assembly of compact KB mirrors that makes this image alignment possible has been accomplished for the first time, as described in this article. For image separations of 9 mm, along the strip, the corresponding image-to-image time separation is 60 ps. The sampling time interval can be decreased to 15 ps by using cables that delay the pulses to the strips by 15-ps intervals. This has been achieved in the instrument described in this work known as KBFRAMED.

The 16-Image KB Optic

The design of a 16-image KB microscope was originally put forth by Marshall, Oertel, and Walsh.[12] In this design, mirrors were cut so they would fit together in a perfect 16-sided polygon, i.e., a hexadecagon. The resulting array of image locations falls on a circle; therefore, a framing camera with circular photocathode strips is needed to frame these images. Subsequently, Marshall[13] proposed a modification to the ideal hexadecagon arrangement of the mirrors that would allow images to be relocated to fall on the rectangular strips of the modern high-speed framing-camera design.[6] The KB mirror focus [Eq. (1)] is given by

$$\frac{1}{p}+\frac{1}{q}=\frac{2}{R\sin i}, \tag{1}$$

where p is the distance from object to mirror, q is the mirror image distance, R is the mirror radius of curvature, and i is the angle of incidence of x rays at the mirror center. The basic concept is to simultaneously move and tilt the mirror, maintaining the focus condition while repositioning the image (Fig. 150.27). The pattern of 16 images can in this way be repositioned to fall on the cathode strips of a high-speed framing camera that are nominally 9.0 mm apart [see Fig. 150.28(a)]. For a mirror pair, each mirror obeys a separate focus equation[14] with small differences for small mirrors. That effect will be neglected in

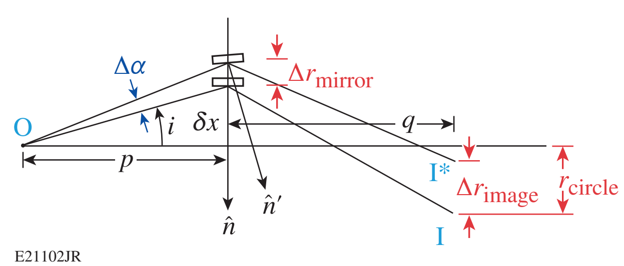

Figure 150.27
Schematic illustrating how of Kirkpatrick–Baez (KB) mirror pairs are repositioned to move an image while maintaining focus. For emission from an object (O), the image is formed at I before repositioning, and I* after repositioning.

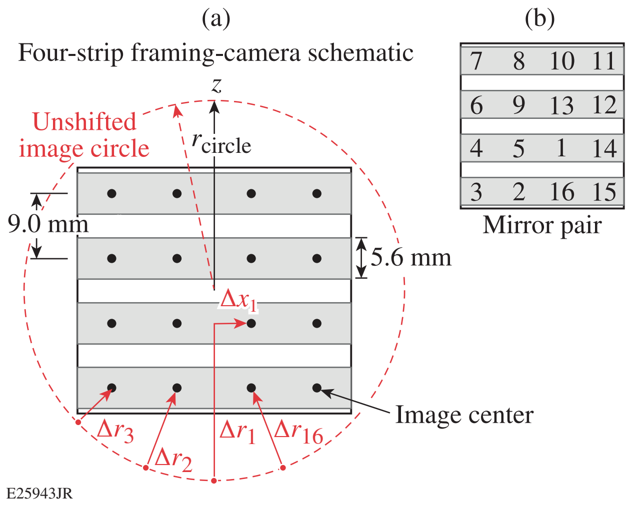

Figure 150.28
(a) Framing-camera image pattern and illustration of relocation of KB image to this pattern. (b) Mirror pair associated with each image location in (a).

this work, and the focus equation will be assumed to apply to the mirror pair, with the center of the pair taken as its location along the optic axis. For a given magnification $M = q/p$, the KB focus equation can be re-expressed as

$$q = \sqrt{M(M+1)R\delta x}, \tag{2}$$

where δx is the offset of a single mirror pair perpendicular to the z axis.

For untilted mirror pairs, the images fall on a circle r_{circle} given by

$$r_{\text{circle}} = \sqrt{2}\,\delta x(M-1). \tag{3}$$

The images of the ideal framing-camera pattern have three different offsets from the center of the pattern [Fig. 150.28(a)]. Four images are at the corners, eight images are on the sides, and four images are at the center of the pattern. The amounts that a mirror pair must be moved, Δr_{mirror}, and tilted in pitch, $\Delta\alpha_{\text{mirror}}$, to move the image by Δr_{image} are given by

$$\Delta r_{\text{mirror}} = \Delta r_{\text{image}}/(M+1), \tag{4}$$

$$\Delta\alpha_{\text{mirror}} = \Delta r_{\text{image}}/p. \tag{5}$$

The parameters of the compact KB mirrors used in this work are given in Table 150.I. The angles ϕ that the mirror pairs make with the axis of the framing camera and the mirror-pair positions and tilts that generate the pattern of image positions shown in Fig. 150.28(b) are provided in Table 150.II. Note that to move the inner images sideways, the mirrors must be tilted in roll $\Delta\beta_{\text{mirror}}$ by an amount

$$\Delta\beta_{\text{mirror}} = \Delta x_{\text{image}}/2q, \tag{6}$$

where Δx_{image} is the perpendicular amount to move the image. As an example, Δx_1 is shown in Fig. 150.28(a).

The mirror-pair alignment is accomplished by placing the mirror-pair vertex at the offset positions given by the values in Table 150.II with preimposed tilts in pitch and roll. This was accomplished by using precision positioning stages and

Table 150.I: Parameters of compact mirrors used in the assembly of the KBFRAMED optic.

R_{KB}	27.5 m
Δt	4.5 mm
Δx	2.2 mm
M	12
q	2173.2 mm
p	181.0 mm
r_{circle}	34.22 mm
i	0.696°

Table 150.II: Mirror-pair offsets and tilts needed to generate the image locations in Fig. 150.28(a) with the pair assignments shown in Fig. 150.28(b). The remaining 12 pairs have common positions and tilts depending on image location as described in the text.

Mirror Pair	ϕ (°)	r_{image} (mm)	Δr_{image} (mm)	Δr_{mirror} (mm)	$\Delta\alpha_{\text{pitch}}$ (°)	$\Delta\beta_{\text{roll}}$ (°)
16	–22.5	14.61	19.61	1.51	0.478	0
1	0	4.5	29.72	2.29	0.725	0.059
2	+22.5	14.61	19.61	1.51	0.478	0
3	+45	19.09	15.13	1.16	0.367	0

a rotary stage to position the base under a fixed, magnified viewing system (157× on a video display). Assembled mirror pairs with pre-applied, UV-curable epoxy on the optic base side were held in place over the base with a vacuum chuck that was positioned by a six-axis positioner (three axes of position and three of tilt). In this fashion the mirrors were cured into place with the UV epoxy acting as the tilted interface to the flat optic base. Positioner accuracies were 1/10,000th of an inch (2.54 μm), 0.01° in rotation of the optic base, and 2.36 arcsec in pitch and roll of the mirror pair.

All mirror-pair image positions were measured by placing the optic assembly in a vacuum system with a microscope chassis identical to that used with the framing camera and back-illuminating a grid co-aligned with the axis of the microscope (z axis) and at the focus distance for $M = 12$ (181 mm) with an e-beam–generated x-ray source. Exposures were taken using a Fuji image plate and image positions determined to 0.1 mm. Any inaccuracies in image positions were minimized by removing the mirror pair and correcting the tilt angles in pitch and roll. Final accuracies of mirror-pair alignments were ~5 μm in position and ~20 arcsec in pitch and roll. This resulted in all images being within 1 mm of the center of the ideal framing-camera cathode strip pattern (i.e., spaced by 9 mm vertically).

The resolution of the mirror pairs at best focus and the off-axis aberrations are discussed in detail in Ref. 13, and the resolution is calculated ideally to be better than ~5 μm over a 400-μm-diam region around best focus. Tilting and repositioning the mirrors, ideally, avoids any additional blurring caused by misalignment from best focus; whereas, in practice, exact alignment is not possible and the framing camera will add additional blurring to the images. Therefore, it is better to determine the resolution by measurement. The inferred point-spread function (PSF), including blurring by the framing camera, is discussed in the next section.

The fused-silica compact KB mirror components are coated with 500 Å of Ir on top of a 150-Å Cr sticking layer as detailed in Ref. 13. The mean radius of curvature of the set of 32 mirrors used to assemble the 16 mirror pairs is 27.2 m, with a range from 25.6 to 28.6 m. The mirror pairs have radii of curvature that are typically within 0.1 m of each other. The x-ray reflectivity[13] of the mirrors has been measured to approach an ideal reflector at the grazing angle of 0.7°. The typical sensitive energy band of the 16-image KB, calculated from the Henke-scattering factors,[15] is shown in Fig. 150.29, including the transmission of the blast shield, vacuum window, and example filters. The sensitive band extends from ~2 keV to 8 keV.

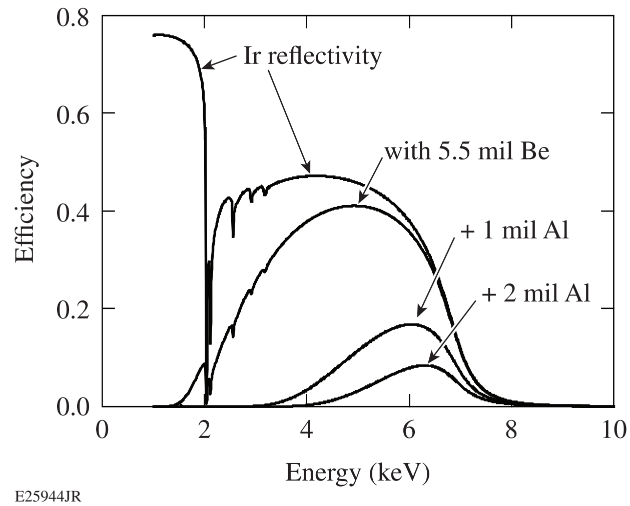

Figure 150.29
KB mirror-pair throughput efficiency including mirror-pair reflectivity, transmission of blast shield and vacuum window, and select filters.

The KBFRAMED Instrument

Figure 150.30 shows a schematic of the KBFRAMED instrument. It consists of a chassis fixed in the OMEGA target chamber, the 16-image KB mirror assembly, and the vacuum interface to a high-speed framing camera.[6] The mirror assembly is held such that the mirror-pair centers are 181 mm from target chamber center, having been set to a precision of 10 μm by a pointer placed on the optic cover when it was installed. A blast cover with holes aligned with the mirror-pair centers contains an x-ray–transparent Be foil that protects the mirrors from exposure to laser-generated target debris. A vacuum Be window separates the chamber vacuum from the path to the image plane, so a separate vacuum system provides a high vacuum (~10^{-6} Torr) to the framing-camera active-detector

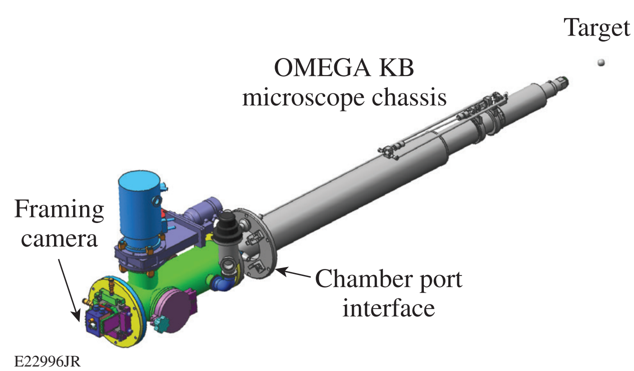

Figure 150.30
Schematic of the KBFRAMED instrument.

region. This also isolates the camera from contaminants such as tritium from the targets. At present, the images are recorded on film that is not in the vacuum region of the framing camera, making it easy to exchange.

Figure 150.31 shows example images of a resolution grid taken by backlighting a grid placed at target chamber center by an Au foil placed 5 mm behind the grid. The foil is illuminated with 2 kJ of 351-nm UV light in a 1-ns pulse from six OMEGA beams. The grid (25.4-μm-diam Cu wires, spaced by 50.8 μm) is placed on a Ta foil with a 500-μm-diam hole, thereby producing 16 clearly separated images. The framing-camera images were recorded with Kodak T-MAX 3200 film and digitized on a calibrated PerkinElmer photo microdensitometer using 20- $\times$ 20-μm scan pixels. A step wedge was imposed on the film before exposure in the framing camera, which allowed the scanned film density to be converted to intensity.[16] The framing camera adds blurring to the images with a scale of ~50-μm full width at half maximum (FWHM) at the image plane, (i.e., ~5 μm at the target plane). To estimate the effective blurring, a step pattern with the width and spacing of the Cu wires is convolved with a 2-D Gaussian blur function and then compared with the observed blurring. Figure 150.32 shows a lineout through a single intensity-corrected image taken through the central 200-μm-wide region, averaged 10 μm vertically to reduce noise. The measured pattern is compared to the Gaussian-blurred step pattern (dashed red curve) whose FWHM is 6 μm. The close agreement indicates that the Gaussian blur function is a good approximation to the net blurring of the framed, KB mirror-pair images.

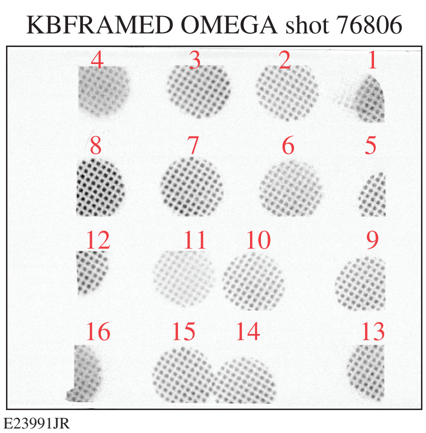

Figure 150.31
Example framed images obtained with KBFRAMED of a backlit grid (25.4-μm-diam Cu wires, spaced by 50.8 μm) taken with a high-speed framing camera.

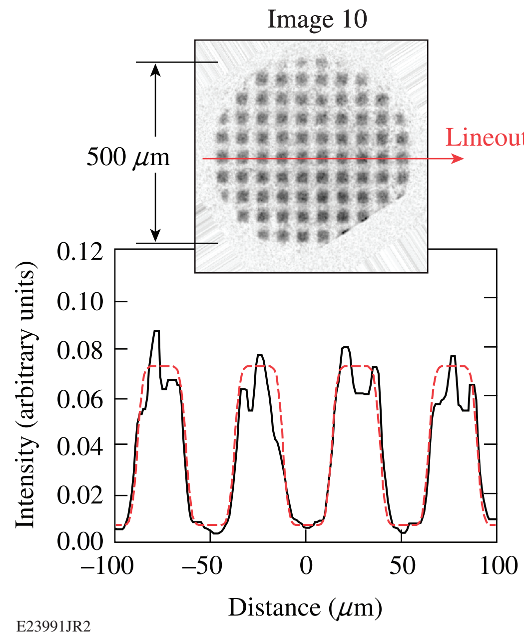

Figure 150.32
Lineout through a single framed, backlit image obtained with KBFRAMED (image 10 of Fig. 150.31). The lineout (solid curve) through the central 200 μm is compared with an ideal grid pattern convolved with a 6-μm FWHM Gaussian blur function (dashed red curve).

Hot-Spot Evolution Imaged by KBFRAMED

KBFRAMED was developed principally to acquire time-resolved x-ray images of the cryogenic target implosion's stagnation region (i.e., hot spot). Triggering of the framing camera is accomplished by electrical delay using a reference to the master oscillator of the OMEGA laser that is accurate to the picosecond level. Since the hot spot evolves very quickly in time (~100 ps), the framing-camera strip times are set to differ by 15 ps from strip to strip by using timed cables whose pulse propagation time differs by this amount (to within ±2 ps, measured to ±1 ps). The relative time of an image is determined from these delays and from the distance of the image from the beginning of the strip, assuming a pulse propagation speed of $c/2$. Deviations from the above assumptions caused by cross talk between neighboring strips are assumed to be small for these small offsets in pulse arrival times.[17] Absolute times can be assigned to data where the simultaneously measured time history of the neutron emission is measured by the neutron temporal diagnostic (NTD);[18] it is assumed that the x-ray and neutron emissions peak at the same time. Figure 150.33 shows example images of a cryogenic target's stagnation recorded by KBFRAMED with times so assigned from the beginning to the end of measureable core emission (the relative times are accurate to ~2 ps, whereas the absolute time may be in error

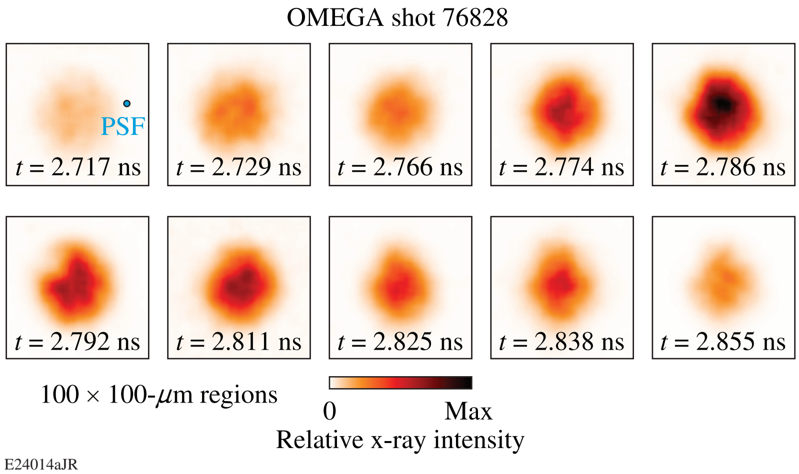

Figure 150.33
KBFRAMED images of hot-spot x-ray emission from a cryogenic target implosion. The approximate point-spread function (PSF) (6-μm FWHM Gaussian) is indicated by a circle of that size in the first image.

by as much as ~50 ps because of uncertainties in the time of the peak of the measured x-ray flux and the absolute timing of NTD). Image signal levels were adjusted for gain as a function of position on the strip determined from measurements of a uniformly illuminated x-ray–emitting foil observed with the same framing camera and the same strip timings. In this experiment an 8.8-μm-thick deuterated polystyrene (CD) shell, 960 μm in diam, filled with DT cryogenically cooled to form a 57-μm-thick DT ice layer, was imploded with 29 kJ of UV (351 nm) from the 60 beams of the OMEGA Laser System,[3] using a triple-picket pulse, having a 1.5-ns-long main pulse.[19] The data were recorded with a 2-mil (50.8-μm) Al filter in front of the framing camera, so the energy band was ~4 to 8 keV (see Fig. 150.29). The emission is seen to start as a low-intensity diffuse emission in a region of ~50-μm diameter, brighten to a maximum in ~70 ps, and then decrease over the next 70 ps. Inferences of hot-spot pressures are made from the size of the hot spot measured by KBFRAMED, the time of fusion burn, the measured ion temperature, and the measured neutron yield.[20] Without every one of these measurements, including the high-spatial-resolution framed images provided by KBFRAMED, the inferences of hot-spot pressure would not be possible. Additionally, the structure evident in the images at scales comparable to the PSF (6-μm FWHM, as indicated by a circle of that size in Fig. 150.33) would not be observable without the resolution provided by KBFRAMED.

An example shape analysis of the hot-spot x-ray emission near the peak of the signal is shown in Fig. 150.34. The hot spot is first fit to a super-Gaussian ellipse convolved with the Gaussian point-spread function given by

$$I'(x,y) = \mathrm{PSF}(x,y) \otimes I_0 \exp\left\{-\left[\left(x^*/a\right)^2 + \left(y^*/b\right)^2\right]^{\eta/2}\right\}, \quad (7)$$

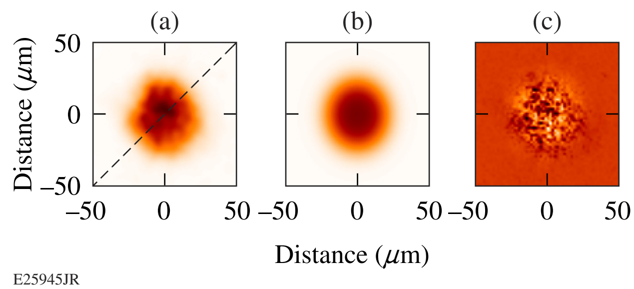

Figure 150.34
A single KBFRAMED cryogenic target hot-spot image at x-ray maximum: (a) image with dashed line indicating direction of lineout, (b) convolved, super-Gaussian–ellipse fit to image, and (c) difference between (a) and (b).

where $\otimes$ denotes convolution, a and b are the lengths of the semi-major and semi-minor axes, respectively, I_0 is the peak value, and η is the super-Gaussian order. The values x^* and y^* are the coordinates lying along the major and minor axes of the ellipse, given by

$$\begin{aligned} x^* &= \left(x - x_c\right)\cos\alpha + \left(y - y_c\right)\sin\alpha, \\ y^* &= \left(x - x_c\right)\sin\alpha - \left(y - y_c\right)\cos\alpha, \end{aligned} \quad (8)$$

where x and y are the coordinates in the image, α is the phase angle to the major axis of the ellipse with respect to the x axis, and x_c and y_c are the locations of the center of the ellipse. Figure 150.34(a) shows the KBFRAMED image at the peak of the hot-spot emission. Figure 150.34(b) shows the best-fit, convolved super-Gaussian ellipse with $a = 23.5$ μm, $b = 20.9$ μm, $\eta = 2.96$, $I_0 = 0.32$, and $\alpha = 91.4°$. Figure 150.34(c) shows the difference, demonstrating that the fit accurately determines the size of the image with only small-scale structure and noise remaining. An example lineout through the image is shown in

Fig. 150.35 with the direction of the lineout indicated by the dashed line in Fig. 150.34(a). The need to use a fit is exemplified by the lineout, where it is evident that in order to estimate the average peak of the hot spot in the presence of noise in the image, it is necessary to use the best-fit value rather than a single peak value. The minimal difference in the convolved fitting function and the inferred super-Gaussian ellipse is because the emission is well resolved by the given resolution of KBFRAMED for this hot-spot size. However, since this method makes it possible to compare sizes when measured with differing resolutions, it is the preferred procedure. With the peak of the hot spot so defined, the size of the hot spot is then defined by the convention that the hot-spot radius is given by the average radius where the emission is 17% of the maximum.[21] With this definition, r_{17} is given by

$$r_{17} = (-\ln 0.17)^{1/\eta} r_0, \tag{9}$$

where r_0 is the geometric mean of a and b $\left(r_0 = \sqrt{ab}\right)$. For the image above, r_{17} is found to be 26.9 μm.

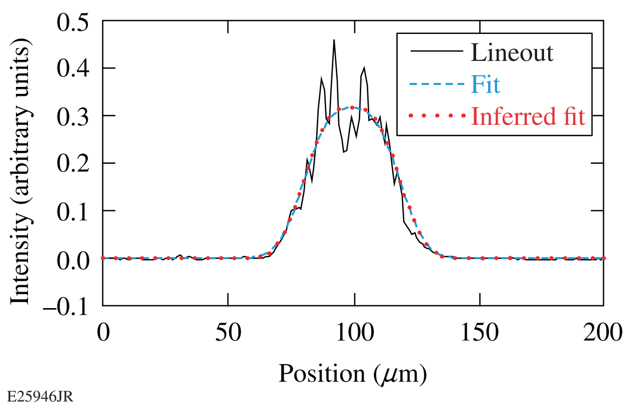

Figure 150.35
Lineout through image in Fig. 150.34(a) and through the convolved super-Gaussian ellipse fit to that image (fit) and through the unconvolved fit (inferred fit).

A more-detailed fit to the hot-spot envelope is determined by fitting the contour of the image at 17% of the fit peak to a Legendre polynomial with the axis of the fit taken as the semi-major axis of the super-Gaussian fit. Figure 150.36 shows the 17% contour, the Legendre fit to the contour (the two sides of the image are separately fit with the major axis of the super-Gaussian fit defining the sides), and the super-Gaussian–fit 17% contour on the image of Fig. 150.34(a). The fractional-radial deviation (departure from a circle) of the contours as a function of angle from the semi-major axis is plotted in Fig. 150.37. The Legendre modes of the fit are shown in Fig. 150.38 for modes from 2 to 10 (mode 1 is just a shift of the center) with the value taken as the average of the fits to the two sides of the contour and the error bar defined by the minimum and maximum of

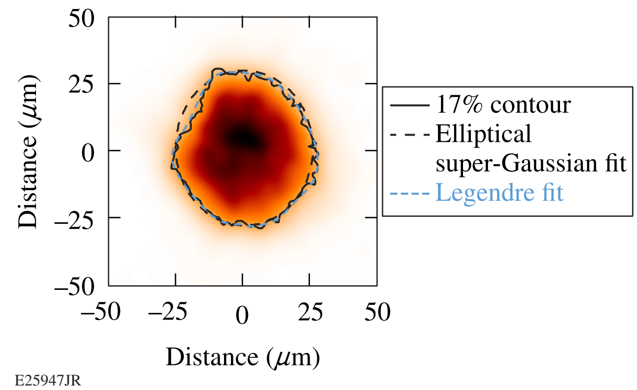

Figure 150.36
Single KBFRAMED image from Fig. 150.34(a) with r_{17} contours superposed.

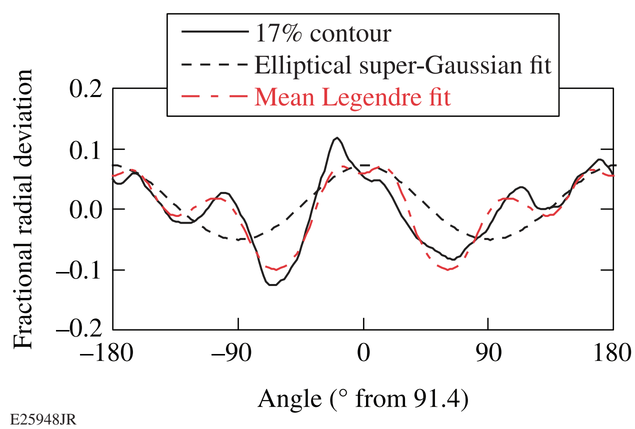

Figure 150.37
Fractional-radial deviation of r_{17} contours from Fig. 150.36 as a function of the angle from the semi-major axis of the super-Gaussian–ellipse fit.

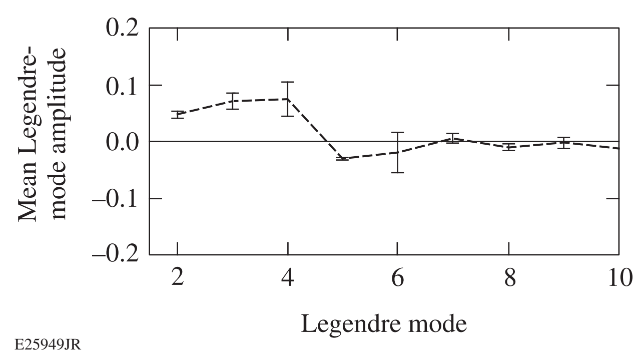

Figure 150.38
Legendre-mode spectrum of the fit to the measured r_{17} contour in Fig. 150.36.

those two fits. The Legendre fit to the hot-spot envelope at r_{17} is, as expected, closer to the observed shape, although the average radius differs only slightly from the elliptical fit (26.7 μm for the observed and Legendre fit as opposed to 26.9 μm for the elliptical fit). In this particular image, modes 2 through 5 are significant although all are less than 0.1 (i.e., less than 10%), whereas modes 6 through 10 are less than ~2%. Note that with an emission region of this radius, mode 10 is expected to be suppressed by the resolution of the instrument by approximately a factor of 2, i.e., the true limit for mode 10 is less than ~4% for an observed limit of ~2%.

The dominant modes of the hot-spot envelope are those expected from on-target illumination nonuniformities coming from beam-intensity imbalance,[22] but this observation does not determine that they are the source of the perturbations. Also, it is important to note that the major axis of the ellipse is within 2° of the vertical (91.4° best fit), which is approximately parallel to the direction of the stalk that holds the cryogenic target in place in the OMEGA target chamber (KBFRAMED is located 10° below the equator of the OMEGA chamber and the stalk direction is downward in the images). The stalk and the glue spot that binds the stalk to the CD shell that surrounds the DT ice layer are known to be the largest mass perturbation at the surface of the target. The effect of a stalk is complex in nature[23] but, simply put, it causes the hot spot to become elongated in the direction of the stalk. This example serves to illustrate the benefit of the increased resolution of the KBFRAMED instrument and the type of information that can be obtained from these images.

Conclusions

A novel 16-image KB microscope design that couples to a high-speed framing camera has been implemented on the OMEGA Laser System. This instrument, known as KBFRAMED, obtains framed images of x-ray emission from laser-generated plasmas with ~6-μm spatial resolution, ~30-ps time resolution over a region of ~400 μm in the energy band from 2 to 8 keV. It was specifically designed to measure the stagnation region (hot spot) of cryogenically cooled DT target implosions that have typical sizes of ~60-μm diameter and durations of ~100 ps. The spatial resolution and time sampling of KBFRAMED allow one to measure the time-varying size and shape of these hot spots.

ACKNOWLEDGMENT

The authors acknowledge the support of the staff at the University of Rochester's Laboratory for Laser Energetics and of the Omega Laser Facility. This material is based on work supported by the Department of Energy National Nuclear Security Administration under Award Number DE-NA0001944, the University of Rochester, and the New York State Energy Research and Development Authority.

REFERENCES

1. P. Kirkpatrick and A. V. Baez, J. Opt. Soc. Am. **38**, 766 (1948).
2. J. F. McGee and J. W. Burrows, Proc. SPIE **106**, 107 (1977).
3. T. R. Boehly, D. L. Brown, R. S. Craxton, R. L. Keck, J. P. Knauer, J. H. Kelly, T. J. Kessler, S. A. Kumpan, S. J. Loucks, S. A. Letzring, F. J. Marshall, R. L. McCrory, S. F. B. Morse, W. Seka, J. M. Soures, and C. P. Verdon, Opt. Commun. **133**, 495 (1997).
4. M. C. Richardson *et al*., IEEE J. Quantum Electron. **QE-19**, 1861 (1983).
5. F. J. Marshall, M. M. Allen, J. P. Knauer, J. A. Oertel, and T. Archuleta, Phys. Plasmas **5**, 1118 (1998).
6. D. K. Bradley *et al*., Rev. Sci. Instrum. **66**, 716 (1995).
7. F. J. Marshall and P. B. Radha, Rev. Sci. Instrum. **85**, 11E615 (2014).
8. F. J. Marshall and J. A. Oertel, Rev. Sci. Instrum. **68**, 735 (1997).
9. L. A. Pickworth *et al*., Rev. Sci. Instrum. **85**, 11D611 (2014).
10. E. I. Moses *et al*., Phys. Plasmas **16**, 041006 (2009).
11. S. Yi *et al*., Rev. Sci. Instrum. **87**, 103501 (2016).
12. F. J. Marshall, J. A. Oertel, and P. J. Walsh, Rev. Sci. Instrum. **75**, 4045 (2004).
13. F. J. Marshall, Rev. Sci. Instrum. **83**, 10E518 (2012).
14. F. J. Marshall and Q. Su, Rev. Sci. Instrum. **66**, 725 (1995).
15. B. L. Henke, E. M. Gullikson, and J. C. Davis, At. Data Nucl. Data Tables **54**, 181 (1993).
16. J. P. Knauer, R. Betti, D. K. Bradley, T. R. Boehly, T. J. B. Collins, V. N. Goncharov, P. W. McKenty, D. D. Meyerhofer, V. A. Smalyuk, C. P. Verdon, S. G. Glendinning, D. H. Kalantar, and R. G. Watt, Phys. Plasmas **7**, 338 (2000).
17. L. R. Benedetti *et al*., Rev. Sci. Instrum. **83**, 10E135 (2012).
18. C. Stoeckl, R. Boni, F. Ehrne, C. J. Forrest, V. Yu. Glebov, J. Katz, D. J. Lonobile, J. Magoon, S. P. Regan, M. J. Shoup III, A. Sorce, C. Sorce, T. C. Sangster, and D. Weiner, Rev. Sci. Instrum. **87**, 053501 (2016).
19. P. B. Radha, J. A. Marozas, F. J. Marshall, A. Shvydky, T. J. B. Collins, V. N. Goncharov, R. L. McCrory, P. W. McKenty, D. D. Meyerhofer, T. C. Sangster, and S. Skupsky, Phys. Plasmas **19**, 082704 (2012).
20. S. P. Regan, V. N. Goncharov, I. V. Igumenshchev, T. C. Sangster, R. Betti, A. Bose, T. R. Boehly, M. J. Bonino, E. M. Campbell, D. Cao, T. J. B. Collins, R. S. Craxton, A. K. Davis, J. A. Delettrez, D. H. Edgell, R. Epstein, C. J. Forrest, J. A. Frenje, D. H. Froula, M. Gatu Johnson, V. Yu. Glebov, D. R. Harding, M. Hohenberger, S. X. Hu, D. Jacobs-

Perkins, R. T. Janezic, M. Karasik, R. L. Keck, J. H. Kelly, T. J. Kessler, J. P. Knauer, T. Z. Kosc, S. J. Loucks, J. A. Marozas, F. J. Marshall, R. L. McCrory, P. W. McKenty, D. D. Meyerhofer, D. T. Michel, J. F. Myatt, S. P. Obenschain, R. D. Petrasso, R. B. Radha, B. Rice, M. Rosenberg, A. J. Schmitt, M. J. Schmitt, W. Seka, W. T. Shmayda, M. J. Shoup, III, A. Shvydky, S. Skupsky, A. A. Solodov, C. Stoeckl, W. Theobald, J. Ulreich, M. D.Wittman, K. M. Woo, B. Yaakobi, and J. D. Zuegel, Phys. Rev. Lett. **117**, 025001 (2016); **117**, 059903(E) (2016).

21. C. Cerjan, P. T. Springer, and S. M. Sepke, Phys. Plasmas **20**, 056319 (2013).

22. F. J. Marshall, J. A. Delettrez, R. Epstein, R. Forties, R. L. Keck, J. H. Kelly, P. W. McKenty, S. P. Regan, and L. J. Waxer, Phys. Plasmas **11**, 251 (2004).

23. I. V. Igumenshchev, F. J. Marshall, J. A. Marozas, V. A. Smalyuk, R. Epstein, V. N. Goncharov, T. J. B. Collins, T. C. Sangster, and S. Skupsky, Phys. Plasmas **16**, 082701 (2009).